applied sciences

MDPI

Article

A Hybrid Prediction Model for Local Resistance Coefficient of Water Transmission Tunnel Maintenance Ventilation Based on Machine Learning

Dawei Tong, Haifeng Wu, Changxin Liu *, Zhangchao Guo and Pei Li

State Key Laboratory of Hydraulic Engineering Simulation and Safety, Tianjin University, Tianjin 300072, China; tongdw@tju.edu.cn (D.T.); wuhaifeng@tju.edu.cn (H.W.); 2021205099@tju.edu.cn (Z.G.); 1022205037@tju.edu.cn (P.L.)

* Correspondence: changxin_liu@tju.edu.cn

Abstract: Multiple ducts in the working shaft and main body of tunnels form a combined tee structure. An efficient and accurate prediction method for the local resistance coefficient is the key to the design and optimization of the maintenance ventilation scheme. However, most existing studies use numerical simulations and model experiments to analyze the local resistance characteristics of specific structures and calculate the local resistance coefficient under specific ventilation conditions. Therefore, there are shortcomings of low efficiency and high cost in the ventilation scheme optimization when considering the influence of the local resistance. This paper proposes a hybrid prediction model for the local resistance coefficient of water transmission tunnel maintenance ventilation based on machine learning. The hybrid prediction model introduces the hybrid kernel into a relevance vector machine to build the hybrid kernel relevance vector machine model (HKRVM). The improved artificial jellyfish search algorithm (IAJS), which utilizes Fuch chaotic mapping, lens-imaging reverse learning, and adaptive hybrid mutation strategies to improve the algorithm performance, is applied to the kernel parameter optimization of the HKRVM model. The results of a case study show that the method proposed in this paper can achieve the efficient and accurate prediction of the local resistance coefficient of maintenance ventilation and improve the prediction accuracy and prediction efficiency to a certain extent. The method proposed in this paper provides a new concept for the prediction of the ventilation local resistance coefficient and can further provide an efficient prediction method for the design and optimization of maintenance ventilation schemes.

Keywords: water transmission tunnel; maintenance ventilation; combined tee structure; local resistance coefficient; improved artificial jellyfish search algorithm; hybrid kernel relevance vector machine

Citation: Tong, D.; Wu, H.; Liu, C.; Guo, Z.; Li, P. A Hybrid Prediction Model for Local Resistance Coefficient of Water Transmission Tunnel Maintenance Ventilation Based on Machine Learning. *Appl. Sci.* **2023**, *13*, 9135. https://doi.org/10.3390/app13169135

Academic Editors: Pedro J. S. Cardoso, João M. F. Rodrigues and Cristina Portalés Ricart

Received: 19 June 2023
Revised: 1 August 2023
Accepted: 7 August 2023
Published: 10 August 2023

1. Introduction

In order to alleviate the water shortage in some economically developed areas and meet the increasing demand for economic development, a large number of long-distance water transfer projects have been built all over the world [1]. With the rapid development of deep underground tunnel construction technology, in order to reduce damage to the production processes, life, and ecological environment of the cities along the project, a deep-buried long-distance water transmission tunnel is utilized as the main water transport buildings in many water diversion projects, some of which are combined with open channels, aqueducts, and other water transport structures for water distribution. According to the literature reports, the hot and humid climate in some areas is suitable for the growth of shellfish and other aquatic organisms, which often invade water transmission tunnels, resulting in reduced water transmission efficiency [2,3]. Therefore, in order to ensure the normal operation of long-distance water transmission projects, it is necessary to carry out regular maintenance.

A number of working shafts are arranged along deep-buried long-distance water transmission tunnels, and water stop valves are arranged in the working shafts. During operation, the water stop valves are closed, and the pipeline is in a state of full pressure flow and isolated from the external natural environment. During maintenance, the water stop valves in the working shaft along the tunnel will be opened to drain water, and the ventilation equipment will be arranged in the working shaft for ventilation during maintenance [4]. The working shafts along the tunnel form a complete ventilation circuit with the main body of tunnels to provide fresh air for maintenance workers, and exhaust the harmful gases released by the biological death and decay in the tunnel and the exhaust fumes from the maintenance machinery, so as to improve the maintenance working environment in the tunnel. Therefore, it is of great significance to scientifically and reasonably design ventilation schemes for long-distance water transmission tunnels during maintenance to ensure the safety of maintenance work. The combined tee structure composed of multiple air ducts in the working shaft and the main body of the tunnel is quite different from the local tee structure in traffic tunnels, mine roadways, and other underground structures. After the high-speed airflow from the air ducts in the working shafts enters the tunnel, the air particles collide with each other in the local area due to the sudden change in the flow direction and the overflow section, resulting in a large local resistance loss. Therefore, the local resistance characteristics and an accurate calculation of the local resistance coefficient of the combined tee structure are the key problems to be solved in the design of maintenance ventilation schemes for long-distance water transmission tunnels.

The essence of local resistance loss is that due to the change in the flow direction and cross-section, fluid particles collide and friction in the local area, forming local eddy currents, resulting in local resistance loss. In hydraulics, the water flow has a large local head loss at the bend, reducer, and tee structures in pipelines, and many scholars have carried out significant amounts of research on local head loss [5,6]. In order to ensure the ventilation effect and reduce energy consumption, scholars have carried out a lot of research on the resistance characteristics of local components in urban traffic tunnels, mine laneways, utility tunnels, and other underground structures and air-conditioning ventilation systems. Wang et al. [7] analyzed the influence of the area ratio, bifurcation angle, flow ratio, and bending radius on the local resistance coefficient of highway tunnel components such as the tee, variable diameter, and bending structure using a numerical simulation method. Wang et al. [8] established a 1:50 bifurcated tunnel scale model based on the prototype of Xiamen Haicang Submarine Tunnel, carried out model experiments to analyze and study the airflow characteristics, and obtained the influence law of the split ratio and the length-to-height ratio of the bifurcation structure on the local loss coefficient. Liang et al. [9] analyzed the influence rules of five traffic parameters, including the distribution of lanes, vehicle distance, blockage ratio, vehicle speed, and proportion of large-scale vehicles, on the vehicle air-resistance coefficient, targeting the influence rules of traffic conditions on the ventilation and pollutant discharge effect of urban traffic tunnels. Wang et al. [10] used a numerical simulation to analyze the local flow field characteristics of a louvered windshield in mine roadways at different opening angles, and derived the local resistance coefficient relation of a louvered windshield. Li et al. [11] established a 1:5 utility tunnel scale model and conducted model experiments under different conditions of the air volume, pipe diameter, and pipe layout to obtain the variation rule of the local resistance at the inlet and outlet of an integrated corridor ventilation system. A two-factor analysis of variance was used to analyze the significance of the influence of the Reynolds number, air volume, and the proportion of the pipeline area ratio. Wang et al. [12] studied the law of influence of the guide vane on the local pressure loss of an air duct elbow through a model experiment and numerical simulation and carried out optimization research on an elbow guide vane.

It can be seen from the above studies that numerical simulations and model experiments are the main methods used to study the ventilation local resistance. However, numerical simulations and model experiments have disadvantages such as a low calculation accuracy, low efficiency, and high cost of human and material resources, and numerical

simulation methods also largely depend on grid division, the selection of the turbulence model, and governing equation-solving methods. Moreover, measurement and human operation errors are unavoidable in the model experiment. Therefore, there are many scholars in the field of fluid mechanics using machine-learning methods to carry out relevant research [13–15], using the black box model of machine learning to replace complex physical mechanisms in fluid mechanics, to overcome the shortcomings of numerical simulations and model-testing methods. Li et al. [16] used ridge regression, decision tree, random forest, gradient boosting regression tree, and other machine-learning methods to predict the average wind pressure and fluctuating wind pressure of high-rise buildings. Zhu et al. [17] conducted research on the surface wind pressure of low-rise buildings, obtained the surface wind pressure under different wind forces by using numerical simulation methods, established a surrogate model based on machine learning, and applied it to optimize the placement of building surface pressure sensors. Hu et al. [18] used adaptive neural-fuzzy inference system, support vector machine, M5 model tree, least-squares support vector machine, and other intelligent prediction models to predict the overflow coefficient of curved pipelines, establishing the mapping relationship between the upstream water head, overflow ratio, curvature, and overflow coefficient. Wakes et al. [19] used machine-learning algorithms to predict dune movement patterns under different wind conditions, providing a technical reference for predicting sediment migration paths. Rushd et al. [20] used artificial neural networks to predict the pressure loss of crude oil transport pipelines, taking the pipe diameter, average flow rate, oil–water density, oil–water viscosity, and water content as the input parameters. In the field of mine roadways, some scholars have also carried out research on ventilation resistance coefficient prediction. Liu et al. [21] established a BP neural network prediction model for the roadway ventilation resistance coefficient and applied the prediction results to the mine ventilation network model. Based on the least-square method, Gao et al. [22] proposed a mathematical model to determine the ventilation resistance coefficient of mines using the inversion of the air volume and node pressure data, and adopted a genetic algorithm and particle swarm algorithm to solve the ventilation resistance coefficient inversion optimization problem.

The main idea of the application of machine learning in the field of fluid mechanics is to establish a high-dimensional mapping relationship between the input parameters and output targets through machine-learning algorithms, replacing the complex physical mechanism of fluid mechanics. The most critical part is obtaining the training sample set. In order to ensure the accuracy and efficiency of the prediction, accurate predictions of the ventilation local resistance coefficient should be obtained by using as few numerical simulation or model test results as possible. In addition, the ventilation local resistance coefficient is related to complex turbulent motion in the local area and has strong nonlinear fluctuation characteristics due to the comprehensive influence of both structural and ventilation parameters. Therefore, the prediction of the ventilation local resistance coefficient is a typical small sample nonlinear prediction problem. Relevance vector machine (RVM) is a sparse kernel method based on the Bayesian framework proposed by Tipping [23]. Its structure is similar to that of support vector machine (SVM), but its training speed is faster, and it has a strong advantage in nonlinear small sample prediction problems. Therefore, the RVM model has been widely used in engineering fields such as mechanical service-life prediction [24], slope deformation probability prediction [25], short-term power coincidence prediction [26], industrial fault classification [27], and pollutant concentration prediction [28]. However, a single-kernel RVM model cannot accurately excavate the deep nonlinear fluctuation characteristics of engineering data. Therefore, the hybrid kernel function is introduced into the RVM model to balance the global generalization ability and local learning ability and improve the prediction accuracy and generalization performance of the model. At the same time, the choice of kernel parameters for the HKRVM model will affect the prediction accuracy of the model. Scholars use swarm intelligent optimization algorithms such as the grey wolf optimization algorithm [29], grasshopper optimization algorithm [30,31], particle swarm optimization algorithm [32], whale optimization

algorithm [33], and bat optimization algorithm [34] to optimize the kernel function of the HKRVM model. The artificial jellyfish search algorithm (AJS) [35], as a swarm intelligent optimization algorithm proposed in recent years, has fewer adjustment parameters and a simple search process. It has been successfully applied in the fields of power grid energy scheduling [36,37], medical image segmentation [38], civil structure engineering [39], and construction engineering image recognition [40]. The application results show that the AJS algorithm has a better optimization accuracy and optimization efficiency than other swarm intelligent optimization algorithms, but the AJS algorithm suffers from premature convergence and can easily fall into local optimal problems when solving high-dimensional nonlinear optimization problems.

In summary, the local resistance coefficient of water transmission tunnel maintenance ventilation is one of the key parameters to be considered in the design of ventilation schemes, and it is related to the complex turbulent movement of fluid. In order to achieve the efficient and accurate prediction of the ventilation local resistance coefficient, this paper proposes a hybrid prediction model for the local resistance coefficient of water transmission tunnel maintenance ventilation, and establishes a mapping relationship between the structural parameters, ventilation parameters, and ventilation local resistance coefficient, in place of a complex fluid mechanics mechanism. It also provides a theoretical basis and technical reference for the optimization of long-distance water transmission tunnel maintenance ventilation schemes.

The remainder of this paper is organized as follows: In Section 2, the research framework of this paper is put forward. In Section 3, a detailed description of the hybrid prediction model for the local resistance coefficient of water transmission tunnel maintenance ventilation based on machine learning is presented. In Section 4, combined with a water transmission project, a case study is presented to verify the applicability of the method proposed in this paper. In Section 5, the effectiveness and superiority of the proposed method are verified by a comparison of the model prediction performance. In Section 6, the conclusion and prospects of the research results in this paper are presented.

2. Research Framework

In this work, a hybrid prediction model for the local resistance coefficient of water transmission tunnel maintenance ventilation based on machine learning is proposed. The research framework is composed of three steps: the construction of a training sample set, building the IAJS-HKRVM prediction model, and a case study, as shown in Figure 1.

Step 1: Construction of training sample set. Sample points are selected in the input parameter design space, and the cross-section mean speed and pressure under different working conditions are calculated based on the three-dimensional numerical model of the local resistance of water transmission tunnel maintenance ventilation, and then, the local resistance coefficient of maintenance ventilation under different working conditions is obtained. The numerical simulation results are verified to construct the training sample set of the prediction model for the local resistance coefficient of water transmission tunnel maintenance ventilation.

Step 2: IAJS-HKRVM prediction model build. Firstly, a Gaussian kernel function with excellent local learning ability and Sigmoid kernel function with excellent global generalization ability are combined by the weighted method and are introduced into the RVM model to establish the HKRVM model, to accurately excavate the deep nonlinear characteristics of the local resistance coefficient of maintenance ventilation. Secondly, in order to determine the optimal kernel parameters of the HKRVM model, the IAJS algorithm is used to optimize the kernel parameters. Fuch chaotic mapping, lens-imaging reverse learning, and adaptive hybrid mutation strategies are introduced to improve the population initialization and location update methods of the AJS algorithm, so as to overcome the shortcomings of local optimal and premature convergence, to improve the optimization accuracy and efficiency of the algorithm. The performance of the IAJS algorithm is compared with other swarm intelligent optimization algorithms on the benchmark test function.

Finally, the hybrid prediction model for the local resistance coefficient of the combined tee structure of water transmission tunnel maintenance ventilation based on machine learning is established.

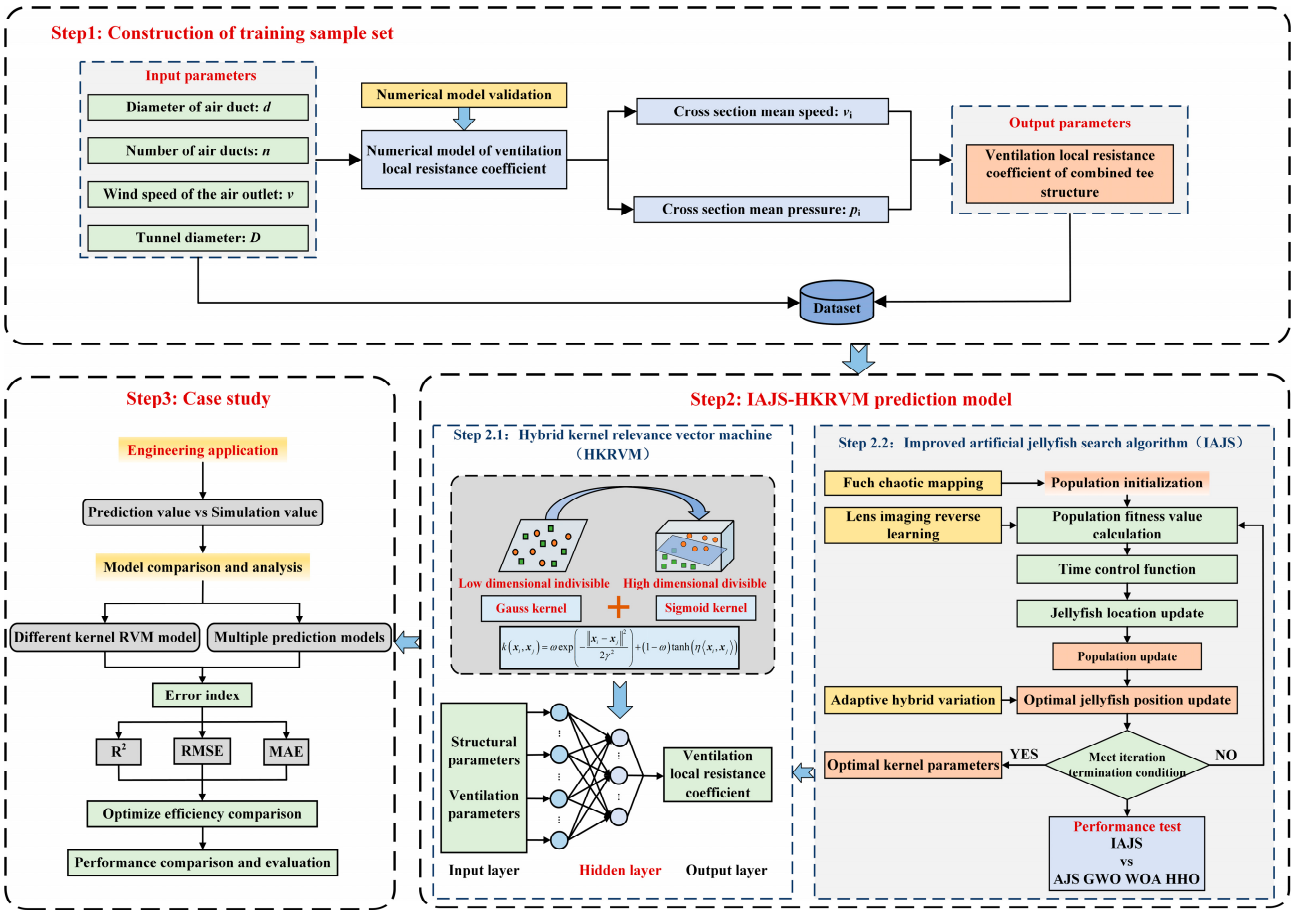

Figure 1. Research framework.

Step 3: Case study. The method proposed in this paper is applied to a long-distance water transmission project and a case study is carried out. Firstly, the results of the numerical simulation and prediction are compared to verify the applicability of the proposed method in this paper. Then, the error indexes such as the relative coefficient square (R^2), mean absolute error (*MAE*), and root mean square error (*RMSE*) are selected to compare the prediction performance of the proposed method in this paper with different kernel RVM models and different prediction models to verify the superiority of the proposed method.

3. Methodology

3.1. IAJS-HKRVM Model

3.1.1. Hybrid Kernel Relevance Vector Machine

The RVM model is a supervised learning method based on a sparse Bayesian framework. Compared with SVM, the RVM model has stronger sparsity and can ensure a good generalization performance with fewer training samples, and its kernel function does not need to meet Mercer conditions. The principle of the RVM model is as follows: the sample dataset obtained by numerical simulation is $S = \{\boldsymbol{x}_n, \boldsymbol{t}_n \mid n = 1, 2, \ldots, N\}$, where N is the number of samples in the dataset, $\boldsymbol{x}_n$ is the input vector, and $\boldsymbol{t}_n$ is the output vector.

Assuming that the prediction target is an independently distributed data sample containing noise, the prediction target is shown in Equation (1).

$$\begin{cases} t_n = y(x_n; \boldsymbol{\omega}) + \xi_n \\ y(\boldsymbol{x}; \boldsymbol{\omega}) = \sum_{n=1}^{N} \omega_n K(\boldsymbol{x}, x_n) + \omega_0 \end{cases} \quad (1)$$

where $\boldsymbol{\omega} = \{\omega_n\}_{n=0}^{N}$ is the model weights vector, ξ_n is the independent Gaussian noise that satisfies distribution $N(0, \sigma^2)$, and $K(\boldsymbol{x}, x_n)$ is the kernel function.

The training process of the RVM model is described as follows: the initial values of the hyperparameters α and σ^2 are set in advance and calculated through several iterations until all parameters meet the convergence conditions. After the iteration is terminated, the hyperparameters are updated to $\boldsymbol{\alpha}_{\mathrm{MP}}$ and σ_{MP}^2 [23]. When the sample to be predicted is x^*, the distribution of the prediction result is shown in Equation (2).

$$p\left(t^* | \boldsymbol{t}, \boldsymbol{\alpha}_{MP}, \sigma_{MP}^2\right) = \int p\left(t^* \middle| \boldsymbol{\omega}, \sigma_{MP}^2\right) p\left(\boldsymbol{\omega} \middle| t, \boldsymbol{\alpha}_{MP}, \sigma_{MP}^2\right) \mathrm{d}\boldsymbol{\omega} = N\left(t^* \middle| y^*, (\sigma^*)^2\right) \quad (2)$$

where $y^* = \mu^{\mathrm{T}} \varphi(x^*)$, $(\sigma^*)^2 = \sigma_{MP}^2 + \varphi(x^*)^{\mathrm{T}} \Sigma \varphi(x^*)$, μ is the mean of the Gaussian distribution, Σ is the variance of the Gaussian distribution, φ is the matrix of the kernel function, $\boldsymbol{\alpha}_{\mathrm{MP}}$ and σ_{MP}^2 are the hyperparameter estimate value corresponding to the maximum marginal likelihood function obtained by the maximum likelihood method, and y^* is the prediction value.

The choice of kernel function and kernel parameter of the RVM model will affect the prediction accuracy. When the sample data features are related to physical laws with deep nonlinear fluctuation characteristics, it is difficult for the single-kernel RVM model to obtain the deep nonlinear fluctuation features of the sample. The local resistance characteristics of water transmission tunnel maintenance ventilation are complicated, which are affected by the structural parameters, ventilation parameters, and other parameters, and are related to complex turbulent movement in the local area and have strong nonlinear fluctuation characteristics. Therefore, the single-kernel RVM model is difficult to be able to achieve the efficient and accurate prediction of the local resistance coefficient of maintenance ventilation. In this paper, a Gaussian kernel function with strong local learning ability and Sigmoid kernel function with strong global generalization ability are combined in a weighted way to establish the HKRVM model for predicting the local resistance coefficient of water transmission tunnel maintenance ventilation. The expression of the hybrid kernel function is shown in Equation (3).

$$k(x_i, x_j) = \lambda \exp\left(-\frac{\|x_i - x_j\|^2}{2\gamma^2}\right) + (1 - \lambda)\tanh\left(\eta \langle x_i, x_j \rangle\right) \quad (3)$$

where λ is the weight coefficient of the kernel function, γ and η are the parameters of the Gaussian kernel function and Sigmoid kernel function.

3.1.2. Improved Artificial Jellyfish Search Algorithm

The AJS algorithm is a new swarm intelligence optimization algorithm proposed in 2021 [35]. The algorithm solves the optimization problem by simulating the natural laws of jellyfish movement and foraging behavior in the ocean and swarm. The algorithm-solving process is shown in Equation (4), and the algorithm's schematic diagram is shown in Figure 2. The algorithm determines the motion form of the jellyfish through the time control mechanism and updates the position of the jellyfish according to the food content of the location of the jellyfish. The motion form of the jellyfish includes the movement of the jellyfish following the ocean current, active movement, and passive movement in the jellyfish swarm. When the time control function $c(t) \geq 0.5$, the position of the jellyfish population changes with the direction of the ocean current movement. When the time

control function $c(t) < 0.5$, the jellyfish move in the jellyfish swarm to update their position. When rand $(0, 1) > 1 - c(t)$, the jellyfish update their positions randomly in the jellyfish swarm according to their spatial range. When rand $(0, 1) \leq 1 - c(t)$, the jellyfish update their positions according to the food content of different jellyfish locations in the swarm [35].

$$\begin{cases} \text{Time control}: c(t) = \left|\left(1 - \frac{t}{T}\right) \times (2 \times \text{rand}(0,1) - 1)\right| \\ \text{Ocean motion} \begin{cases} \overrightarrow{\text{trend}} = X^* - \beta \times \text{rand}(0,1) \times \mu \\ X_i(t+1) = X_i(t) + \text{rand}(0,1) \times \overrightarrow{\text{trend}} \end{cases}, c(t) \geq 0.5 \\ \text{Passive motion}: X_i(t+1) = X_i(t) + \gamma \times \text{rand}(0,1) \times (U_b - L_b), \text{rand}(0,1) > 1 - c(t) \\ \text{Active motion} \begin{cases} X_i(t+1) = X_i(t) + \text{rand}(0,1) \times \overrightarrow{\text{Direction}} \\ \overrightarrow{\text{Direction}} = \begin{cases} X_j(t) - X_i(t), f(X_i) \geq f(X_j) \\ X_i(t) - X_j(t), f(X_i) < f(X_j) \end{cases} \end{cases}, \text{rand}(0,1) \leq 1 - c(t) \end{cases} \quad (4)$$

where t is the current iteration, T is the maximum number of iterations, $\overrightarrow{\text{trend}}$ is the ocean trend, X^* is the optimal jellyfish location in the current iteration, β is the distribution coefficient that is related to the length of $\overrightarrow{\text{trend}}$, and its value is 3, μ is the mean location of all jellyfishes, γ is the motion coefficient that is related to the length of motion around the locations of jellyfishes, and its value is 0.1, U_b and L_b are, respectively, the upper and lower bounds of the search space, $X_i(t)$ and $X_j(t)$ are, respectively, the i and j jellyfish locations in the current iteration, and $f(X_i)$ and $f(X_j)$ are, respectively, the food content of the location of the i and j jellyfish, that is, the fitness value.

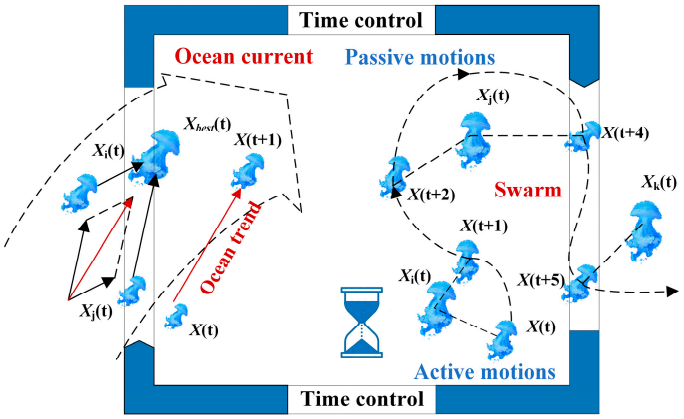

Figure 2. Diagram of artificial jellyfish search algorithm [35].

In order to overcome the shortcomings of the AJS algorithm, such as premature convergence and local optimization, this paper introduces Fuch chaotic mapping, lens-imaging reverse learning, and adaptive hybrid mutation strategy to improve the AJS algorithm.

The AJS algorithm uses logistic chaotic mapping to generate the initial population, but the initial population generated by logistic chaotic mapping is concentrated in the edge of the space, which makes it difficult to search for the optimal solution quickly and reduces the optimization efficiency of the algorithm. Fuch chaotic mapping is an infinite folding chaotic mapping, which has a better ergodic, dynamic, and convergence than finite folding chaotic mapping such as logistic mapping and tent mapping [41]. The initial population generated by Fuch chaotic mapping is concentrated in several local areas, which enables a rapid population search. In this paper, Fuch chaotic mapping is used to generate chaotic sequences, and then the chaotic sequences are mapped into the design parameter space to

generate the initial jellyfish population. The Fuch chaotic mapping expression is shown in Equation (5).

$$x(t+1) = \cos\left[1/x(t)^2\right] \tag{5}$$

where $x(t) \neq 0$, $x \in Z+$, $t = 1, 2, \cdots, T$.

In order to further illustrate the differences between the two chaotic mapping methods, the scatterplot and histogram of the two chaotic mapping sequences are compared, respectively. Figure 3 shows the histogram and scatter diagram of logistic chaotic mapping and Fuch chaotic mapping. As shown in Figure 3, variables generated by logistic chaotic mapping are distributed centrally in the edge region of the design space, while variables generated by Fuch chaotic mapping are distributed centrally in a small range and dispersed in a large range. Therefore, using Fuch chaotic mapping to generate the initial population can make the population quickly concentrate in the optimal solution region, reduce the number of algorithm iterations, and improve the optimization efficiency of the population.

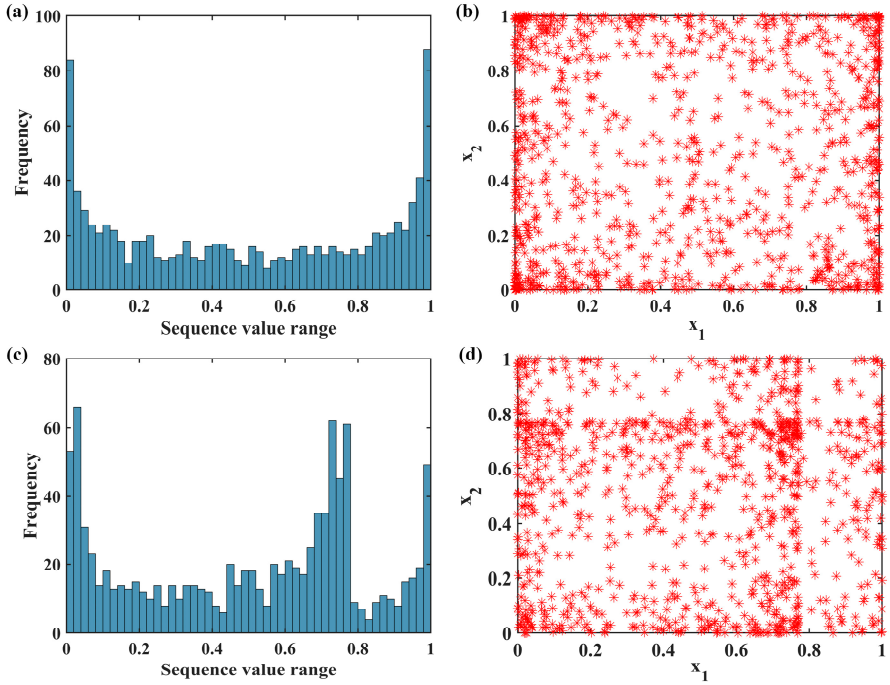

Figure 3. (**a**) Histogram of logistic chaotic mapping sequence; (**b**) scatter diagram of logistic chaotic mapping sequence; (**c**) histogram of Fuch chaotic mapping sequence; (**d**) scatter diagram of Fuch chaotic mapping sequence.

Lens-imaging reverse learning is a reverse-learning strategy inspired by the principle of convex lens imaging. Its scaling factor changes nonlinearly and dynamically with the number of iterations. The equations are as follows:

$$x_j'^* = \frac{U_{bj} + L_{bj}}{2} + \frac{U_{bj} + L_{bj}}{2k} - \frac{x_j^*}{k} \tag{6}$$

$$k = k_{\max} - (k_{\max} - k_{\min}) \cdot (t/T)^2 \tag{7}$$

where k is the scaling factor, U_{bj} and L_{bj} are, respectively, the upper and lower bounds of the j-dimensional components in the search space, x_j^* is the j-dimensional component of the jellyfish, $x_j'^*$ is the j-dimensional component of the jellyfish by lens-imaging reverse learning, $k_{\max}$ and $k_{\min}$ are the maximum scaling factor and minimum scaling factor, respectively, and their values are 10 and 1, respectively.

In this paper, an adaptive hybrid mutation strategy is adopted to mutate the position of the optimal jellyfish obtained in each iteration, and its parameters are dynamically updated with the number of iterations to better balance the ability of the global exploration and local development of the algorithm. The equation for the adaptive hybrid mutation is shown in Equation (8).

$$u_{best}^{t} = x_{best}^{t}(1 + \lambda_1 Cauchy(0,1) + \lambda_2 Gauss(0,1)) \tag{8}$$

where u_{best}^{t} is the location of the current optimal jellyfish after mutation, x_{best}^{t} is the location of the current optimal jellyfish, $Cauchy(0, 1)$ is the random variable that satisfies the Cauchy distribution, $Gauss(0, 1)$ is the random variable that satisfies the Gauss distribution, and $\lambda_1 = 1 - (t/T)^2$ and $\lambda_2 = (t/T)^2$ are the dynamic parameters that change adaptively with the number of iterations.

In order to validate the performance of the improved artificial jellyfish search algorithm, four benchmark test functions are chosen to compare the optimization performance of the IAJS algorithm, the AJS algorithm, Grey wolf optimization algorithm (GWO), Whale optimization algorithm (WOA), and Harris hawks optimization algorithm (HHO). Among them, F1 and F2 are unimodal functions, F3 is a multimodal function, and F4 is a fixed-dimensional multimodal function. The basic parameter settings of each algorithm are shown in Table 1. The other parameters remain the same, the optimization dimension is 30, the population size is 30, and the maximum number of iterations is 500. Table 2 shows the statistical results of the 30 independent tests of each algorithm on the benchmark test functions, where the bold part represents the algorithm with the best optimization performance. Figure 4 shows the average iterative convergence curves on the benchmark test functions.

Table 1. The basic parameter settings of each algorithm.

Algorithm Name	Parameters
IAJS	$\beta = 3$, $\gamma = 0.1$, $k_{\max} = 10$, $k_{\min} = 1$
AJS	$\beta = 3$, $\gamma = 0.1$
GWO	$a_{\max} = 2$, $a_{\min} = 0$, r_1, $r_2 \in [0, 1]$
WOA	$a \in [0, 2]$, r_1, $r_2 \in [0, 1]$, $p = 0.5$, $b = 1$, $l \in [-1, 1]$
HHO	$p = 0.5$, $J \in [0, 2]$

Table 2. The test results of each algorithm on the benchmark test functions.

Function	Statistics	Algorithm				
		IAJS	AJS	GWO	WOA	HHO
F1: Sphere	Optimal	$\mathbf{0.0000} \times 10^{-00}$	2.9132×10^{-19}	4.4427×10^{-29}	3.0818×10^{-86}	3.4871×10^{-111}
	Mean	$\mathbf{0.0000} \times 10^{-00}$	1.5817×10^{-17}	1.9413×10^{-27}	2.2725×10^{-74}	6.6443×10^{-96}
	Standard	$\mathbf{0.0000} \times 10^{-00}$	1.8679×10^{-17}	2.8171×10^{-27}	1.0694×10^{-73}	3.5842×10^{-95}
F2: Schewefel 1.2	Optimal	$\mathbf{0.0000} \times 10^{-00}$	1.9518×10^{-18}	7.6909×10^{-09}	2.1240×10^{-01}	2.4287×10^{-97}
	Mean	$\mathbf{0.0000} \times 10^{-00}$	7.2734×10^{-17}	1.1714×10^{-05}	8.1110×10^{-01}	1.2096×10^{-79}
	Standard	$\mathbf{0.0000} \times 10^{-00}$	8.7846×10^{-17}	2.4667×10^{-05}	3.6620×10^{-01}	3.6922×10^{-79}
F3: Ackley	Optimal	$\mathbf{8.8818} \times 10^{-16}$	1.0691×10^{-10}	7.5495×10^{-14}	8.8818×10^{-16}	8.8818×10^{-16}
	Mean	$\mathbf{8.8818} \times 10^{-16}$	4.6871×10^{-10}	1.0640×10^{-13}	3.9672×10^{-15}	8.8818×10^{-16}
	Standard	$\mathbf{0.0000} \times 10^{-00}$	2.0870×10^{-10}	1.5810×10^{-14}	2.0298×10^{-15}	1.0029×10^{-31}
F4: Six-Hump Camel-Back	Optimal	$\mathbf{-1.0316} \times 10^{-00}$	-1.0316×10^{-00}	-1.0316×10^{-00}	-1.0316×10^{-00}	-1.0316×10^{-00}
	Mean	$\mathbf{-1.0316} \times 10^{-00}$	-1.0316×10^{-00}	-1.0316×10^{-00}	-1.0316×10^{-00}	-1.0316×10^{-00}
	Standard	$\mathbf{0.0000} \times 10^{-00}$	6.4600×10^{-16}	1.6814×10^{-08}	1.0060×10^{-09}	3.5641×10^{-10}

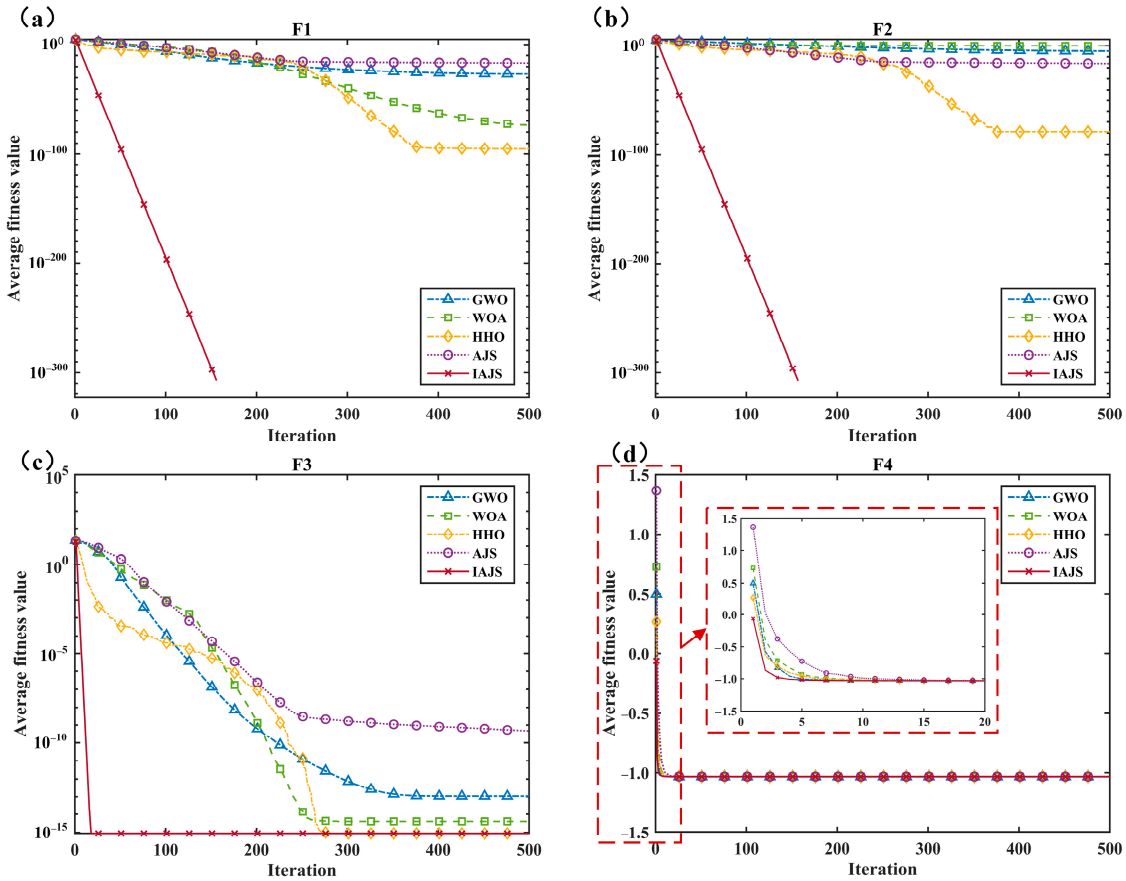

Figure 4. Average iteration convergence curves of each benchmark test function ((**a**)—F1; (**b**)—F2; (**c**)—F3; (**d**)—F4).

As shown in Table 2, the optimization results of the IAJS are superior to the AJS, WOA, GWO, and HHO. The optimal value and average value of the IAJS test results on F1~F2 and F4 can reach the theoretical optimal value, and the standard deviation is 0, but the theoretical optimal value is not reached on F3, because there are many local optimal values in F3, making it easy to fall into the local optimal value. However, the standard deviation of the experiment is 0. Therefore, the optimization performance of the IAJS algorithm has been greatly improved. In addition, it can be seen from Figure 4 that the IAJS algorithm converges faster than the other algorithms, indicating that the IAJS algorithm can jump out of the local optimal faster. Meanwhile, it can be seen from Figure 4a,b that compared with the other four algorithms, the convergence speed and accuracy of the IAJS algorithm are significantly improved. Additionally, it can be seen from Table 2 and Figure 4d that all five algorithms have reached the theoretical optimal solution, but from the convergence curves, the convergence speed of the IAJS algorithm is faster than that of the other four algorithms. Therefore, the AJS algorithm improved by Fuch chaotic mapping, lens-imaging reverse learning, and adaptive hybrid mutation strategy can effectively improve the optimization accuracy and efficiency. Thus, it will be applied to the kernel parameter optimization of the HKRVM model.

3.2. Establishment Process of the Hybrid Prediction Model for Local Resistance Coefficient of Water Transmission Tunnel Maintenance Ventilation Based on Machine Learning

In this section, a hybrid prediction model for the local resistance coefficient of water transmission tunnel maintenance ventilation based on machine learning is proposed, and the model establishment process is shown in Figure 5. The specific steps are as follows:

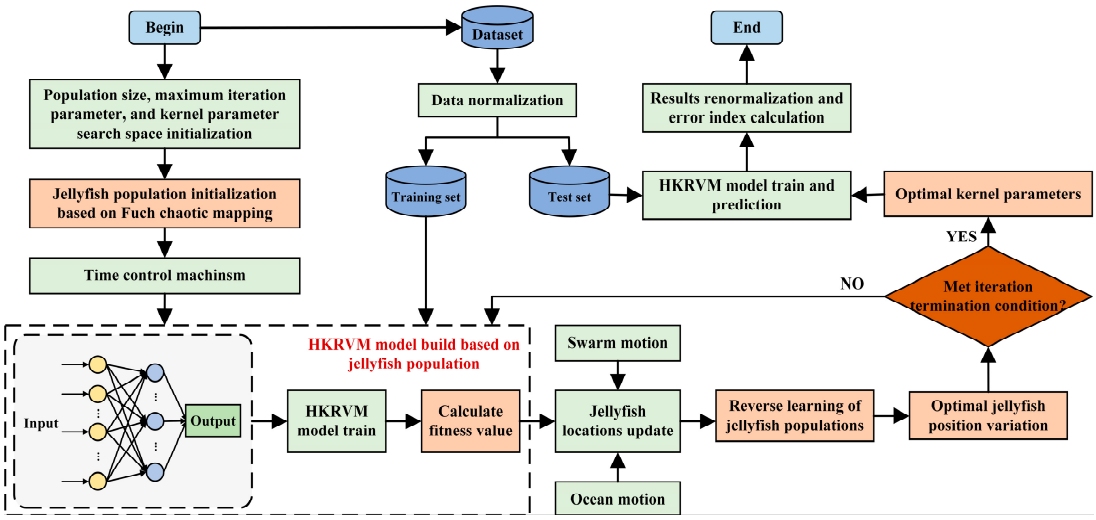

Figure 5. Establishment process of the hybrid prediction model.

(1) The sample set is normalized and the training set and test set are divided according to the ratio of 3:1;

(2) The population size, maximum number of iterations, and kernel parameters the search space, the initial jellyfish population is generated based on Fuch chaotic mapping, the HKRVM model is built based on the jellyfish population, the mean absolute error of prediction is selected as the fitness function and the corresponding fitness value is obtained;

(3) Start iteration. The fitness value of each jellyfish is compared to update the jellyfish location, the optimal jellyfish location X_{gbest} and optimal fitness value $fitness_{best}$ of the jellyfish are determined, and lens-imaging reverse learning and adaptive hybrid variation are carried out on the updated jellyfish population and the current optimal jellyfish, respectively;

(4) Enter the next iteration. The position and fitness value of the optimal individual jellyfish are updated successively until the iteration termination condition is met and then output the optimal jellyfish, that is, the optimal kernel parameters;

(5) The IAJS-HKRVM model is established using the optimal kernel parameters, and the IAJS-HKRVM model is trained. After the model training, the test samples are used for testing and verification, and the prediction results of the local resistance coefficient are obtained, the error index is calculated, and the prediction performance is evaluated.

4. Case Study

The long-distance water transfer project is located in southern China's Guangzhou Province. The total length of the water transmission line is 113.1 km, a deep-buried TBM tunnel is the main water transmission structure, accounting for 75% of the total water transmission line, and the tunnel is buried at a depth of 30 to 60 m. The location of the project and the layout of the TBM tunnel are shown in Figure 6a,b. The TBM tunnel of the project starts from the reservoir and ends at the water pond, with a total length of 28.3 km. Ten working shafts are arranged along the tunnel, numbered 1#~10#, and the tunnel is correspondingly divided into ten parts by working shafts, numbered ①~⑩.

The three-dimensional model of the tunnel and working shafts and maintenance ventilation process are shown in Figure 6c. During the operation of the water transmission tunnel, the water stop valves in the working shaft are closed and in a state of pressure, and the inside of the tunnel is full of water. During maintenance, the water stop valves are opened to discharge the water flow inside the pipeline, and the pipe is kept dry. Ventilation equipment such as axial flow fans and air ducts are arranged in the working shaft for maintenance ventilation, supplying fresh air from the outside into the tunnel (as shown by the solid green line with an arrow in Figure 6c) to ensure maintenance work safety and the working comfort of maintenance personnel.

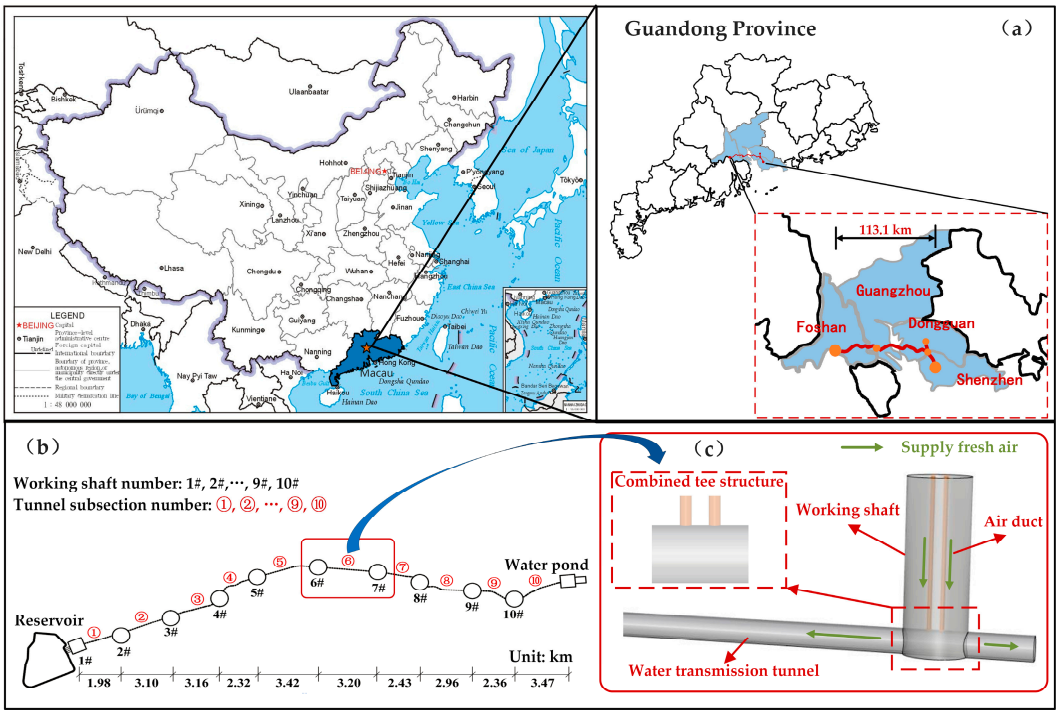

Figure 6. Diagram of engineering layout and maintenance ventilation ((**a**)—The project location diagram; (**b**)—The TBM tunnel layout diagram; (**c**)—Maintenance ventilation process diagram).

4.1. Analysis of Ventilation Local Resistance Characteristics

In this section, a three-dimensional numerical simulation method is used to analyze the ventilation local resistance characteristics of the combined tee structure, and the RNG k-ε turbulence model is used to simulate the complex turbulent motion in the local region of the combined tee structure. The RNG k-ε turbulence model transport equation is based on the standard k-ε turbulence model with an added corresponding source term, which can accurately simulate the complex flow phenomena such as local vortex, jet collision, and high-speed strain flow [42]. In this paper, the outlet of the air duct is set as the velocity inlet boundary, and it is assumed that the airflow distribution of the outlet is uniform and the airflow direction is perpendicular to the section of the outlet. The left and right sides of the tunnel are set as the pressure outlet boundary, and the gauge pressure at the outlet is set to 0. The wall of the tunnel and the wall of the air duct are set as the solid wall boundary without slip [4].

In order to verify the reliability and accuracy of the numerical simulation results, the model experiment results of the local loss coefficient of the bifurcated tunnel under different bifurcation angles in the paper of Zhang et al. [43] are quoted in this paper for comparison and verification, and the local loss coefficient under different bifurcation angles and flow diversion ratios is simulated. The comparison between the numerical simulation and model experiment value is shown in Figure 7. As can be seen from Figure 7, when the bifurcation angle is 5°, the error range of the local loss coefficient is 6.0~13.5% and the average error is 8.9%; when the bifurcation angle is 10°, the error range of the local loss coefficient is 5.3~12.2% and the average error is 8.4%; and when the bifurcation angle is 15°, the error range of the local loss coefficient is 4.2~12.9% and the average error is 7.8%. The error comparison results show that the numerical simulation results are in good agreement with the model test results in the reference [43]. Therefore, the three-dimensional numerical model of the ventilation local resistance of the combined tee structure of the water transmission tunnel can be used to solve the sample point calculation of the prediction model of the ventilation local resistance coefficient based on the IAJS-HKRVM.

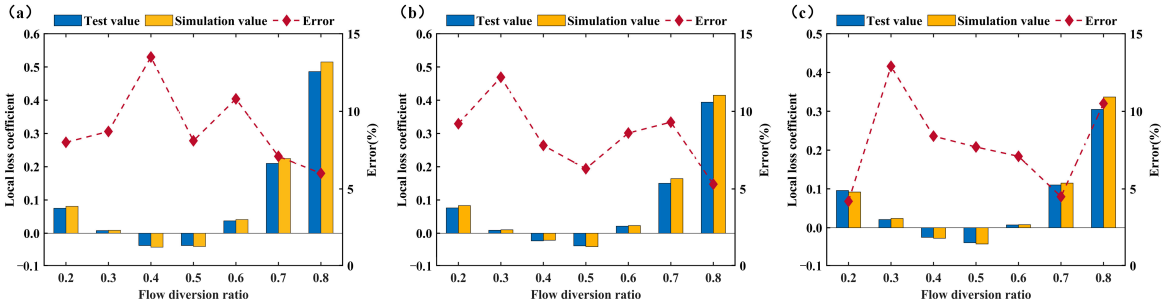

Figure 7. Comparison of local loss coefficient simulation and test value under different bifurcation angles and flow diversion ratios ((**a**)—5°; (**b**)—10°; (**c**)—15°).

In order to analyze the ventilation local resistance characteristics of the combined tee structure, the numerical simulation results with the parameters of an air pipe diameter of 1.2 m, number of air pipes of 4, a tunnel diameter of 8 m, and a wind speed of the outlet of 10 m/s are selected for analysis. Figure 8 shows the wind velocity distribution cloud map and vector map of the central longitudinal section of the combined tee structure under this working condition. After the high-speed airflow emitted from the top air duct outlet enters the tunnel, the flow direction changes sharply under the obstruction of the tunnel wall, and moves and diffuses to both ends, forming the wall-attached flow and collision wall-attached jet, as shown in Figure 8b ① and ②. After the high-speed airflow emitted by the adjacent air pipe enters the tunnel, the overflow section suddenly expands, the turbulent edge develops and diffuses, the airflow reaching the bottom of the tunnel is diverted by the obstructing wall, and the adjacent jets collide with each other to form the local vortex region, as shown in Figure 8b ③. At the same time, after the airflow enters the tunnel, it diffuses to both ends of the tunnel, collides with the airflow in the upper space of the tunnel, and forms the vortex region, as shown in Figure 8b ④. In summary, the local resistance loss is caused by the obstructing wall in the tunnel and the collision of adjacent high-speed jets, which forms many local vortices in the local area.

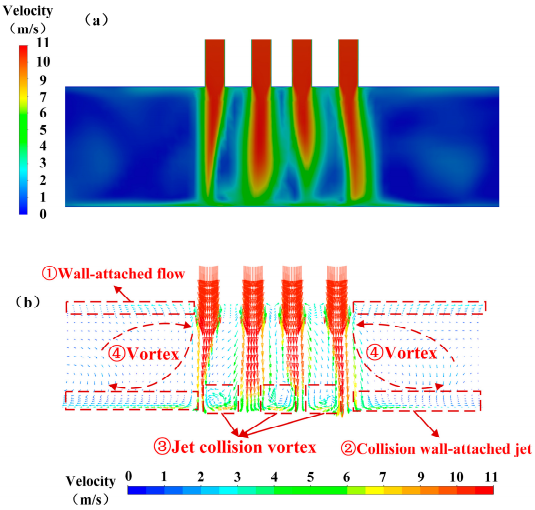

Figure 8. Wind velocity distribution cloud map (**a**) and vector map (**b**) in the longitudinal section of the water transmission tunnel.

4.2. Analysis of Prediction Results for Ventilation Local Resistance Coefficient

Considering the engineering layout, maintenance ventilation characteristics, and local resistance characteristics, the diameter of the tunnel, the diameter of the air duct, the number of the air duct, and the airflow speed of the outlet are selected in this paper as the input variables of the IAJS-HKRVM prediction model, and the local resistance coefficient is selected as the output variable. The values or ranges of each input variable are shown

in Table 3. A total of 68 groups of samples are obtained by random sampling, and the response values of each group of samples are calculated based on the three-dimensional numerical model of maintenance ventilation in Section 4.1. In the numerical simulation process of the 68 groups of samples, their main difference lies in the physical model and the settings of the boundary conditions. Changes in the number of air ducts, the diameter of the air ducts, and the diameter of the tunnel will lead to changes in the physical model, and changes in the airflow speed of the outlet will lead to changes in the setting of the boundary conditions.

Table 3. The values or ranges of each input variable.

Input Variable	Unit	The Values or Ranges
Diameter of air duct	m	1~2
Number of air duct	/	1, 2, 3, 4
Diameter of tunnel	m	5~8
Airflow speed of outlet	m/s	3~10

Among the 68 groups of samples obtained based on the three-dimensional numerical simulation model, 50 groups are randomly selected as the training set, and the other 18 groups are selected as the test set. The local resistance coefficient of water transmission tunnel maintenance ventilation is predicted by the IAJS-HKRVM prediction model established in this paper. The learning curves of the fitness of the train set and test set are shown in Figure 9. The comparison between the prediction results and the numerical simulation results is shown in Figure 10.

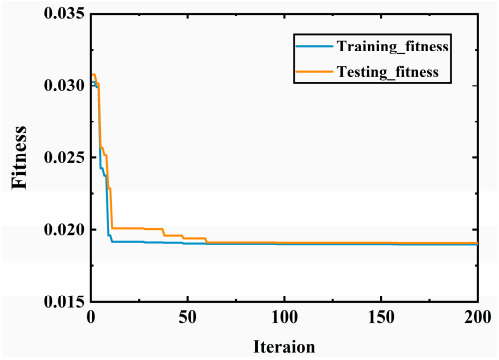

Figure 9. The learning curves of the fitness of train set and test set.

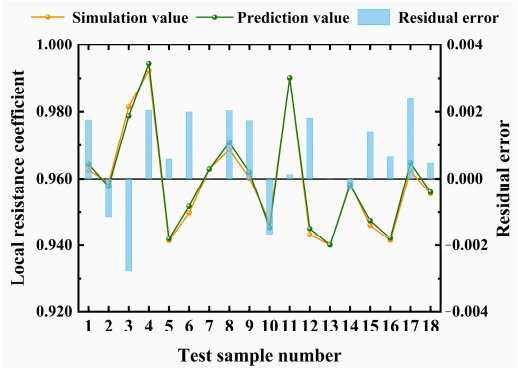

Figure 10. Comparison of local resistance coefficient prediction value and simulation value.

It can be seen from Figure 9 that the fitness function value of the training set is smaller than that of the test set. Moreover, when the model is trained for about 60 iterations, the fitness curves of the training set and the test set begin to converge and there is little difference between the fitness values of the training set and the test set. Therefore, the model has a good generalization ability. As shown in Figure 10, the ventilation local

resistance coefficient of the combined tee structure predicted by the IAJS-HKRVM model has a high consistency with the numerical simulation results, and the residual difference between the predicted value and the simulated value at each test sample point is within the allowable range. Therefore, the hybrid prediction model for the local resistance coefficient of water transmission tunnel maintenance ventilation proposed in this paper can efficiently and accurately predict the local resistance coefficient under different working conditions and can be used to predict the local resistance coefficient of the combined tee structure of the water transmission tunnel.

5. Discussion

In this section, in order to further verify the effectiveness and superiority of the IAJS-HKRVM hybrid prediction model for the local resistance coefficient of water transmission tunnel maintenance ventilation proposed in this paper, the prediction performances of different kernel RVM models and other conventional prediction models are compared by using the residual distribution of each sample point, R^2, *MAE*, *RMSE*, and other error indicators and their improvement rates. The calculation formulas of R^2, *MAE*, and *RMSE* are shown in Equation (9).

$$\begin{cases} R^2 = 1 - \sum_{i=1}^{n} (y_i - \hat{y}_i)^2 / \sum_{i=1}^{n} (y_i - \overline{y}_i)^2 \\ MAE = \frac{1}{n} \sum_{i=1}^{n} |y_i - \hat{y}_i| \\ RMSE = \sqrt{\frac{1}{n} \sum_{i=1}^{n} (y_i - \hat{y}_i)^2} \end{cases} \tag{9}$$

where y_i is the ventilation local resistance coefficient numerical simulation value, $\overline{y}_i$ is the average value of the ventilation local resistance coefficient numerical simulation value, $\hat{y}_i$ is the prediction value of the ventilation local resistance coefficient, and n is the sample number of the test set.

5.1. Comparison with Conventional RVM Models

In order to verify the advantages of the Gaussian and Sigmoid hybrid kernel functions adopted in this paper in balancing the global generalization and local learning abilities, Gaussian kernel (g-RVM), polynomial kernel (p-RVM), Sigmoid kernel (s-RVM), Gaussian and polynomial hybrid kernel (g-p-RVM), and Gaussian and Sigmoid hybrid kernel (g-s-RVM) models are selected to predict the local resistance coefficient, respectively. The boxplot of the prediction residual error of different kernel relevance vector machine models is shown in Figure 11, the prediction error index comparison of the different kernel RVM models is shown in Table 4, and the improvement rate of the prediction error index of the IAJS-HKRVM model compared with different kernel RVM models is shown in Figure 12.

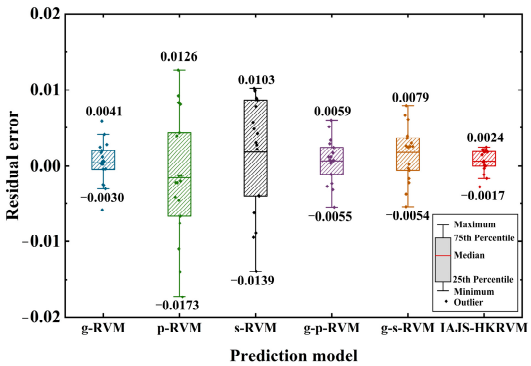

Figure 11. Boxplot of different kernel RVM model prediction residual error.

Table 4. Comparison of different kernel RVM model prediction error indexes.

Model	R^2	*MAE*	*RMSE*
g-RVM	0.9702	0.0021	0.0027
p-RVM	0.7264	0.0067	0.0081
s-RVM	0.7598	0.0069	0.0076
g-p-RVM	0.9662	0.0023	0.0029
g-s-RVM	0.9384	0.0033	0.0039
IAJS-HKRVM	**0.9903**	**0.0013**	**0.0015**

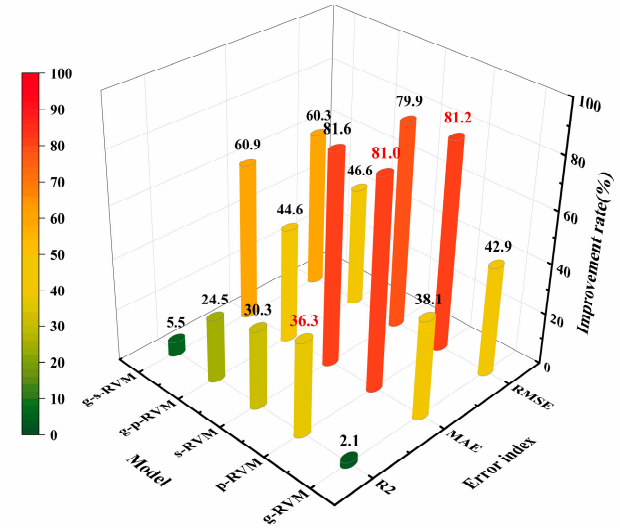

Figure 12. Comparison of different kernel RVM model prediction error index improvement rate.

As can be seen from Figure 11, among the single-kernel RVM models, the Gaussian kernel RVM model has the most concentrated prediction residual error distribution, and the median value is close to zero, which is close to the IAJS-HKRVM model, while the polynomial kernel RVM and Sigmoid kernel RVM model have a scattered prediction residual error distribution. In the hybrid kernel RVM model, the residual error distributions of the Gaussian + polynomial hybrid kernel RVM and Gaussian + Sigmoid hybrid kernel RVM are close, but the prediction accuracy is lower than that of the Gaussian kernel RVM model because the kernel parameters are determined according to experience, which agrees with the error indexes presented in Table 4. Therefore, the IAJS algorithm is used to optimize the kernel parameters of the HKRVM model, which further improves the prediction accuracy. As can be seen from Table 4, the error indexes of the IAJS-HKRVM prediction model are superior to other RVM models with different kernels, and the error indexes of the IAJS-HKRVM prediction model are R^2 (0.9903), *MAE* (0.0013), and *RMSE* (0.0015), respectively.

As can be seen from Figure 12, the numbers marked in red in Figure 12 show the highest improvement rate of each error index of the IAJS-HKRVM model compared with other RVM models with different kernel. The R^2 of the IAJS-HKRVM model has the highest increase of 36.3% compared with the polynomial kernel RVM model, and the lowest increase of 2.1% compared with the Gaussian kernel RVM model. The *MAE* has the largest decrease of 81.0% compared with the polynomial kernel RVM model, and the lowest decrease of 38.1% compared with the Gaussian kernel RVM model. The *RMSE* has the largest decrease of 81.2% compared with the polynomial kernel RVM model, and the lowest decrease of 42.9% compared with the Gaussian kernel RVM model, which agrees with the data presented in Table 4. According to the comparative analysis results, it can be seen that single-kernel RVM models such as the Gaussian kernel, polynomial kernel, and Sigmoid kernel are difficult to be able to effectively mine complex nonlinear motion features. At the same time, it is difficult to guarantee the prediction accuracy and

generalization performance of the model by determining the kernel parameters based on experience. Therefore, the global generalization ability and local learning ability of the Gaussian + Sigmoid hybrid kernel effective equilibrium model adopted in this paper can better explore the nonlinear fluctuation characteristics of the local resistance coefficient of the combined tee structure.

5.2. Comparison with Other Prediction Models

In order to further verify the superiority of the prediction performance of the IAJS-HKRVM model, SVM, backpropagating neural network (BPNN), and the AJS-HKRVM model are selected to predict the ventilation local resistance coefficient, respectively, and are compared with the prediction results of the IAJS-HKRVM model. Among them, the radial basis kernel function is used in the SVM model, and the kernel parameters and penalty factor are determined by grid search. The learning rate of the BPNN is 0.001, and the hyperparameters are determined by Bayesian optimization. The boxplot of the residual error of the prediction results of each model is shown in Figure 13, the prediction error index comparison of each model is shown in Table 5, and the prediction error index improvement rate of the IAJS-HKRVM model compared with other models is shown in Figure 14.

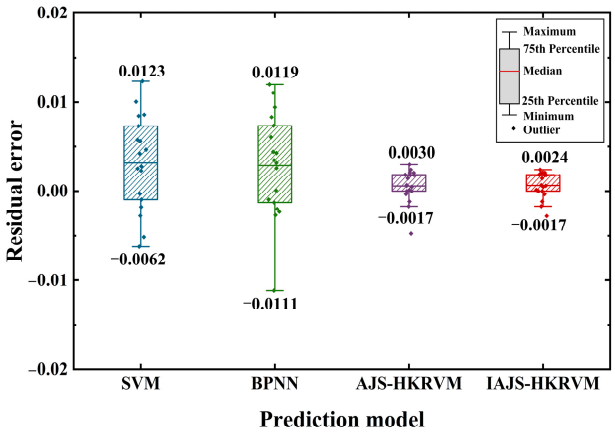

Figure 13. Boxplot of different model prediction residual error.

Table 5. Comparison of other model prediction error indexes.

Model	R^2	*MAE*	*RMSE*
SVM	0.8505	0.0050	0.0060
BPNN	0.8339	0.0051	0.0063
AJS-HKRVM	0.9857	0.0014	0.0019
IAJS-HKRVM	**0.9903**	**0.0013**	**0.0015**

As shown in Figure 13, the maximum and minimum values of the prediction residual error of the IAJS-HKRVM model are lower than those of the other prediction models, and its prediction residual error distribution is the most concentrated, and the median is the closest to 0. The residual error distribution concentration of the AJS-HKRVM model is close to that of the IAJS-HKRVM model, but its maximum residual is slightly larger. The SVM has the second highest degree of prediction residual error distribution concentration, while the BPNN has the lowest degree of prediction residual error distribution concentration, which is consistent with the prediction error indicators of each model in Table 5. As can be seen from Table 5, the error indexes of the IAJS-HKRVM model are better than those of the AJS-HKRVM, SVM, and BPNN. As can be seen from Figure 14, the numbers marked in red in Figure 14 show the highest improvement rate of each error index of the IAJS-HKRVM model compared with other conventional prediction models. The R^2 of the IAJS-HKRVM model has the highest increase of 18.8% compared with the BPNN, and the lowest increase

of 0.5% compared with the AJS-HKRVM model. The *MAE* has the largest decrease of 75.2% compared with the BPNN, and lowest decrease of 11.6% compared with the AJS-HKRVM model. The *RMSE* has the largest decrease of 75.8% compared with the BPNN, and the lowest decrease of 17.7% compared with the AJS-HKRVM model. Therefore, the prediction performance of the IAJS-HKRVM model has been greatly improved compared with other conventional prediction models.

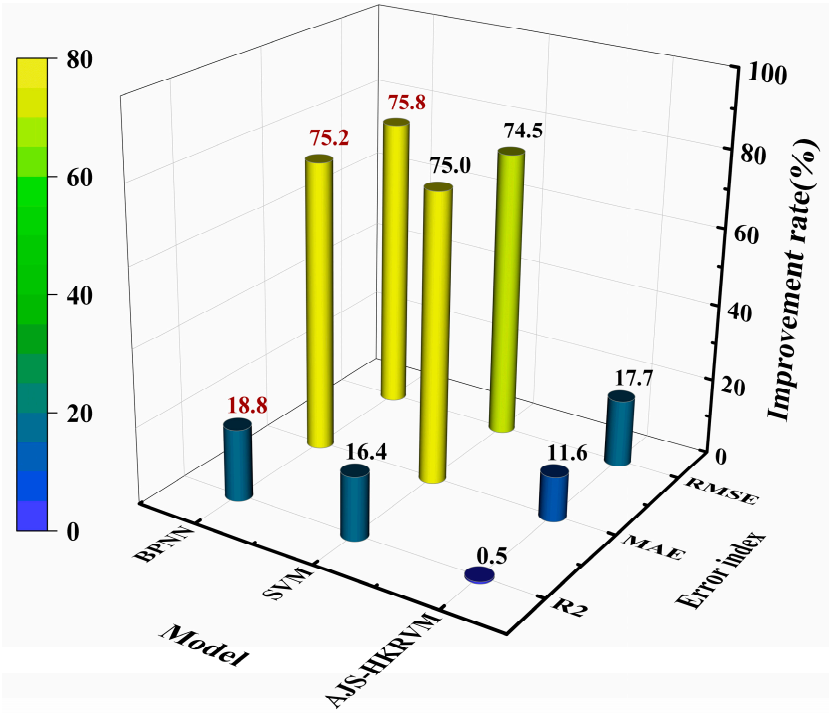

Figure 14. Comparison of prediction error index improvement rate of the IAJS-HKRVM model compared with other models.

As shown in Figures 13 and 14, the prediction accuracy of the IAJS-HKRVM model is only slightly improved compared with the AJS-HKRVM model. Figure 15 shows the comparison of the convergence curves of the AJS-HKRVM and IAJS-HKRVM model. As can be seen from Figure 15, during the first iteration, the average optimal fitness values of the AJS-HKRVM and IAJS-HKRVM model are 0.0424 and 0.0308, respectively. In addition, by the 38th iteration of the IAJS-HKRVM, the jellyfish population has been concentrated in the region near the optimal solution, while the AJS-HKRVM arrived at the region near the optimal solution at the 46th iteration. The running time of each iteration is the same, so the optimization efficiency of the IAJS-HKRVM model is improved by about 17.4% compared with the AJS-HKRVM. Therefore, the artificial jellyfish search algorithm improved by the Fuch chaotic mapping, lens-imaging reverse learning, and adaptive hybrid mutation strategy enables the initial population to quickly concentrate in the optimal solution region, balances the global and local search capabilities, and can quickly jump out of the local optimal, effectively improving the optimization efficiency of the AJS algorithm. Therefore, using the IAJS algorithm to optimize the kernel parameters of the HKRVM model improves the prediction accuracy and generalization ability of the model, and realizes the efficient and accurate prediction of the ventilation local resistance coefficient of the combined tee structure.

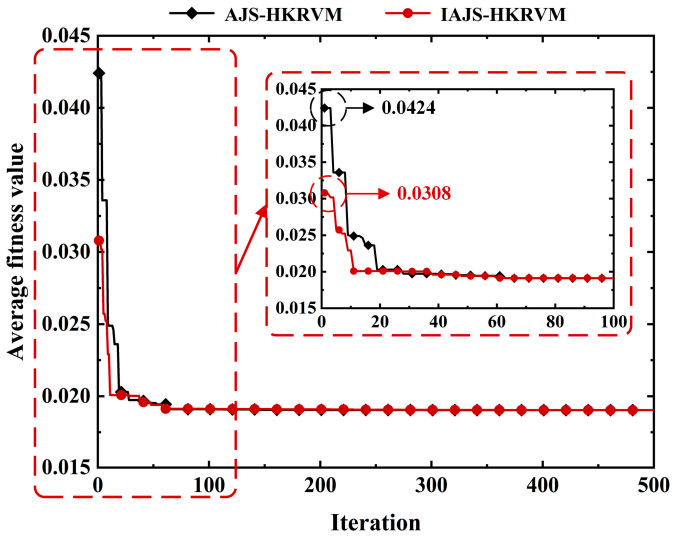

Figure 15. Comparison of convergence curves of IAJS-HKRVM and AJS-HKRVM model.

6. Conclusions

The local resistance characteristics of water transmission tunnel maintenance ventilation are complicated, which is related to the complex nonlinear turbulent motion in the local region. In order to calculate the efficiency and accuracy of the ventilation local resistance coefficient, this paper proposed a hybrid prediction model for the local resistance coefficient of water transmission tunnel maintenance ventilation based on an intelligent optimization algorithm and a small-sample machine-learning method, and established the nonlinear mapping relationship between the structural parameters, ventilation parameters, and local resistance coefficient, so as to replace the complex physical mechanism of fluid mechanics. The main research achievements are as follows:

(1) Research on numerical simulations of the local resistance characteristics of the combined tee structure of water transmission tunnel maintenance ventilation was carried out. As a result, the local resistance characteristics of the combined tee structure were analyzed, determining that the local resistance is mainly caused by the collision and friction of the airflow in the local area and the formation of multiple local eddy currents due to the sudden change in the cross-section and flow direction.

(2) The IAJS-HKRVM hybrid model was proposed. The IAJS algorithm was used to automatically optimize the kernel parameters of the HKRVM model, which effectively improved the prediction accuracy and generalization performance, and the optimization performance of the IAJS algorithm was verified based on the benchmark test function.

(3) Combined with an actual project, the local resistance coefficient of the combined tee structure of water transmission tunnel maintenance was predicted. The results showed that the IAJS-HKRVM model has a good prediction performance and can better excavate the deep nonlinear fluctuation characteristics of the ventilation local resistance coefficient.

(4) The effectiveness and superiority of the proposed method in the prediction of the ventilation local resistance coefficient were verified by comparing and analyzing the prediction performance of different models. In terms of the prediction accuracy, the IAJS-HKRVM model has the highest improvement of 36.3% compared with different kernel RVM models, and the highest improvement of 18.8% compared with other conventional models. In terms of the prediction efficiency, it has improved by about 17.4% compared with the AJS-HKRVM.

In future studies, the local resistance coefficient prediction method for water transmission tunnel maintenance ventilation proposed in this paper will be combined with a multi-objective optimization study of the maintenance ventilation scheme of a long-distance water transmission tunnel, to provide a theoretical basis and technical parameters for the

design and optimization of the maintenance ventilation scheme of a long-distance water transmission tunnel.

Author Contributions: D.T.: methodology, investigation, writing—original draft. H.W.: methodology, data curation, writing—original draft. C.L.: methodology, supervision, writing—review and editing. Z.G.: investigation, validation, supervision. P.L.: investigation, visualization. All authors have read and agreed to the published version of the manuscript.

Funding: This research was funded by [Natural Science Foundation of Tianjin, China] grant number [No. 19JCYBJC22600].

Institutional Review Board Statement: Not applicable.

Informed Consent Statement: Not applicable.

Data Availability Statement: The data supporting the findings of this study are available from the corresponding author upon reasonable request.

Acknowledgments: The authors are grateful for the support from the State Key Laboratory of Hydraulic Engineering Simulation and Safety at Tianjin University.

Conflicts of Interest: The authors declare that they have no known competing financial interests or personal relationships that could have appeared to influence the work reported in this paper.

Abbreviations

HKRVM	Hybrid kernel relevance vector machine
IAJS	Improved artificial jellyfish search algorithm
RVM	Relevance vector machine
AJS	Artificial jellyfish search algorithm
SVM	Support vector machine
BPNN	Backpropagating neural network
R^2	Relative coefficient square
MAE	Mean absolute error
RMSE	Root mean square error
GWO	Grey wolf optimization algorithm
WOA	Whale optimization algorithm
HHO	Harris hawks optimization algorithm

References

1. Zhang, C.; Nong, X.Z.; Shao, D.G.; Zhong, H.; Shang, Y.M.; Liang, J.K. Multivariate water environmental risk analysis in long-distance water supply project: A case study in China. *Ecol. Indic.* **2021**, *125*, 70–82. [CrossRef]
2. Liu, D.M.; Hong, J.; Wang, R.; Cui, F.Y. Current solution to *Limnoperna fortunei* problem in water and pipelines. In Proceedings of the 2011 2nd International Conference on Artificial Intelligence, Management Science and Electronic Commerce (AIMSEC), Dengfeng, China, 8–10 August 2011.
3. Zhang, C.D.; Xu, M.Z.; Wang, Z.Y.; Liu, W.; Yu, D.D. Experimental study on the effect of turbulence in pipelines on the mortality of *Limnoperna fortunei* veligers. *Ecol. Eng.* **2017**, *109*, 101–118. [CrossRef]
4. Liu, C.X.; Wang, X.L.; Tong, D.W.; Liu, Z.; Yang, C.; Chen, S.; Wang, R.N.; Ding, C.Y. Impact of various multishaft combined ventilation modes on the removal of harmful gases released from mussel decay in a long-distance water conveyance tunnel. *Tunn. Undergr. Space Technol.* **2022**, *128*, 104633. [CrossRef]
5. Crapper, M.; Motta, D.; Sinclair, C.; Cole, D.; Monteleone, M.; Cosheril, A.; Tree, J.; Parkin, A. The hydraulic characteristics of Roman lead water pipes: An experimental investigation. *Int. J. Hist. Eng. Technol.* **2022**, *91*, 119–134. [CrossRef]
6. Baselt, I.; Malcherek, A. Determining the Flow Resistance of Racks and the Resulting Flow Dynamics in the Channel by Using the Saint-Venant Equations. *Water* **2022**, *14*, 2469. [CrossRef]
7. Wang, X.; Tan, W.; Ma, J.; Wang, L. Study on local structural resistance of ventilation system in highway tunnels. *Mod. Tunn. Technol.* **2019**, *56*, 104–113. (In Chinese)
8. Wang, X.; Wang, M.N.; Qin, P.C.; Yan, T.; Chen, J.; Deng, T.; Yu, L.; Yan, G.F. An experimental study on the influence of local loss on ventilation characteristic of dividing flow in urban traffic link tunnel. *Build. Sci.* **2020**, *174*, 106793. [CrossRef]
9. Liang, C.J.; Nan, S.; Shao, X.L.; Li, X.T. Calculation method for air resistance coefficient of vehicles in tunnel with different traffic conditions. *J. Build. Eng.* **2021**, *44*, 102971. [CrossRef]

10. Wang, N.; Li, Y.C.; Zhang, H.; Zhang, J.; Li, B.L. Study on flow distribution and local resistance characteristics of louvered windshield. *J. Saf. Sci. Technol.* **2022**, *18*, 118–123. (In Chinese)
11. Li, S.; Liu, X.F.; Wang, J.X.; Zheng, Y.L.; Deng, S.M. Experimental reduced-scale study on the resistance characteristics of the ventilation system of a utility tunnel under different pipeline layouts. *Tunn. Undergr. Space Technol.* **2019**, *90*, 131–143. [CrossRef]
12. Wang, H.D.; Li, X.H.; Tang, Y.; Chen, X.W.; Shen, H.H.; Cao, X.C.; Gao, H.M. Simulation and experimental study on the elbow pressure loss of large air duct with different internal guide vanes. *Build Serv. Eng. Res. Technol.* **2022**, *43*, 725–739. [CrossRef]
13. Li, Y.F.; Chang, J.T.; Kong, C.; Bao, W. Recent progress of machine learning in flow modeling and active flow control. *Chin. J. Aeronaut.* **2022**, *35*, 14–44. [CrossRef]
14. Hammond, J.; Pepper, N.; Montomoli, F.; Michelassi, V. Machine Learning Methods in CFD for Turbomachinery: A review. *Int. J. Turbomach. Propuls. Power* **2022**, *7*, 16. [CrossRef]
15. Mostafa, K.; Zisis, I.; Moustafa, M.A. Machine learning Techniques in Structural Wind Engineering: A state-of-the-art review. *Appl. Sci.* **2022**, *12*, 5232. [CrossRef]
16. Li, Y.; Huang, X.; Li, Y.G.; Chen, F.B.; Li, Q.S. Machine learning based algorithms for wind pressure prediction of high-rise buildings. *Adv. Struct. Eng.* **2022**, *25*, 2222–2233. [CrossRef]
17. Zhu, Q.M.; Zhao, Z.; Yan, J.H. Physics-informed machine learning for surrogate modeling of wind pressure and optimization of pressure sensor placement. *Comput. Mech.* **2022**, *71*, 481–491. [CrossRef]
18. Hu, Z.L.; Karami, H.; Rezaei, A.; DadrasAjirlou, Y.; Piran, M.J.; Band, S.S.; Chau, K.W.; Mosavi, A. Using soft computing and machine learning algorithms to predict the discharge coefficient of curved labyrinth overflows. *Eng. Appl. Comp. Fluid Mech.* **2021**, *15*, 1002–1015. [CrossRef]
19. Wakes, S.J.; Bauer, B.O.; Mayo, M. A preliminary assessment of machine learning algorithms for predicting CFD-simulated wind flow patterns over idealized foredunes. *J. R. Soc. N. Z.* **2021**, *51*, 290–306. [CrossRef]
20. Rush, S.; Rahman, M.; Arifuzzaman, M.; Ali, S.A.; Shalabi, F.; Aktaruzzaman, M. Predicting pressure losses in the water-assisted flow of unconventional crude with machine learning. *Pet. Sci. Technol.* **2021**, *39*, 926–943. [CrossRef]
21. Liu, Y.Q. Study on the air quantity of mine ventilation network based on BP neural network prediction model of friction resistance coefficient in roadway. *Min. Saf. Environ. Prot.* **2021**, *48*, 101–106. (In Chinese)
22. Gao, K.; Deng, L.J.; Liu, J.; Wen, L.X.; Wong, D.; Liu, Z.Y. Study on mine ventilation resistance coefficient inversion based on genetic algorithm. *Arch. Min. Sci.* **2018**, *63*, 813–826.
23. Tipping, M.E. Sparse Bayesian learning and the relevance vector machine. *J. Mach. Learn. Res.* **2001**, *1*, 211–244.
24. Guo, R.X.; Wang, Y.G. Remaining useful life prognostics for the rolling bearing based on a hybrid data-driven method. *Proc. Inst. Mech. Eng. Part I–J Syst. Control Eng.* **2021**, *235*, 517–531. [CrossRef]
25. Pan, Q.J.; Leung, Y.F.; Hsu, S.C. Stochastic seismic slope stability assessment using polynomial chaos expansions combined with relevance vector machine. *Geosci. Front.* **2021**, *12*, 405–414. [CrossRef]
26. Ding, J.; Wang, M.L.; Ping, Z.W.; Fu, D.F.; Vassiliadis, V.S. An integrated method based on relevance vector machine for short-term load forecasting. *Eur. J. Oper. Res.* **2020**, *287*, 497–510. [CrossRef]
27. Huang, J.; Yang, X.; Shardt, Y.A.W.; Yan, X.F. Fault Classification in Dynamic Process Using Multiclass Relevance Vector Machine and Slow Feature Analysis. *IEEE Access* **2020**, *8*, 9115–9123. [CrossRef]
28. Pham, Q.B.; Sammen, S.S.; Abba, S.I.; Mohammadi, B.; Shahid, S.; Abdulkadir, R.A. A new hybrid model based on relevance vector machine with flower pollination algorithm for phycocyanin pigment concentration estimation. *Environ. Sci. Pollut. Res.* **2021**, *28*, 32564–32579. [CrossRef]
29. Qiu, J.S.; Fan, Y.C.; Wang, S.L.; Yang, X.; Qiao, J.L.; Liu, D.L. Research on the remaining useful life prediction method of lithium-ion batteries based on aging feature extraction and multi-kernel relevance vector machine optimization model. *Int. J. Energy Res.* **2022**, *46*, 13931–13946. [CrossRef]
30. Tao, H.; Al-Bedyry, N.K.; Khedher, K.M.; Shahid, S.; Yaseen, Z.M. River water level prediction in coastal catchment using hybridized relevance vector machine model with improved grasshopper optimization. *J. Hydrol.* **2021**, *598*, 126477. [CrossRef]
31. Song, W.S.; Guan, T.; Ren, B.Y.; Yu, J.; Wang, J.J.; Wu, B.P. Real-Time Construction Simulation Coupling a Concrete Temperature Field Interval Prediction Model with Optimized Hybrid-Kernel RVM for Arch Dams. *Energies* **2020**, *13*, 4487. [CrossRef]
32. Zhao, Y.; Li, Z.Q. Import and Export Trade Prediction Algorithm of Belt and Road Countries Based on Hybrid RVM Model. *Math. Probl. Eng.* **2022**, *2022*, 6467326. [CrossRef]
33. Wang, S.; Zhang, X.C.; Chen, W.X.; Han, W.; Zhou, S.B.; Pecht, M. State of health prediction based on multi-kernel relevance vector machine and whale optimization algorithm for lithium-ion battery. *Trans. Inst. Meas. Control*, 2021, *ahead of print*. [CrossRef]
34. Bui, D.T.; Hoang, N.D.; Nguyen, H.; Tran, X.L. Spatial prediction of shallow landslide using Bat algorithm optimized machine learning approach: A case study in Lang Son Province, Vietnam. *Adv. Eng. Inform.* **2019**, *42*, 100978.
35. Chou, J.S.; Truong, D.N. A novel metaheuristic optimizer inspired by behavior of jellyfish in ocean. *Appl. Math. Comput.* **2021**, *389*, 125535. [CrossRef]
36. Shaheen, A.M.; El-Sehiemy, R.A.; Alharthi, M.M.; Ghoneim, S.S.M.; Ginidi, A.R. Multi-objective jellyfish search optimizer for efficient power system operation based on multi-dimensional OPF framework. *Energy* **2021**, *237*, 121478. [CrossRef]
37. Farhat, M.; Kamel, S.; Atallah, A.M.; Khan, B. Optimal Power Flow Solution Based on Jellyfish Search Optimization Considering Uncertainty of Renewable Energy Sources. *IEEE Access* **2021**, *9*, 100911–100933. [CrossRef]

38. Abdel-Basset, M.; Mohamed, R.; Abouhawwash, M.; Chakrabortty, R.K.; Ryan, M.J.; Nam, Y. An improved jellyfish algorithm for multilevel thresholding of magnetic resonance brain image segmentations. *CMC-Comput. Mat. Contin.* **2021**, *68*, 2961–2977. [CrossRef]
39. Chou, J.S.; Liu, C.Y.; Prayogo, H.; Khasani, R.R.; Gho, D.; Lalitan, G.G. Predicting nominal shear capacity of reinforced concrete wall in building by metaheuristics-optimized machine learning. *J. Build. Eng.* **2022**, *61*, 105046. [CrossRef]
40. Chou, J.S.; Karundeng, M.A.; Truong, D.N.; Cheng, M.Y. Identifying deflections of reinforced concrete beams under seismic loads by bio-inspired optimization of deep residual learning. *Struct. Control Health Monit.* **2022**, *29*, e2918. [CrossRef]
41. Fu, W.Y.; Ling, C.D. An adaptive iterative chaos optimization method. *J. Xi'an Jiaotong Univ.* **2013**, *47*, 33–38. (In Chinese)
42. ANSYS Inc. *ANSYS FLUENT Theory Guide*; ANSYS Inc.: Canonsburgp, PA, USA, 2013.
43. Zhang, X.; Zhang, T.H.; Huang, Z.Y.; Zhang, C.; Kang, C.; Wu, K. Local loss and flow characteristic of dividing flow bifurcated tunnel. *J. Zhejiang Univ.* **2018**, *52*, 440–445. (In Chinese)